Space Weather

RESEARCH ARTICLE
10.1029/2018SW001916

Special Section:
Space Weather Events of 4-10 September 2017

SuperDARN Radar-Derived HF Radio Attenuation During the September 2017 Solar Proton Events

Emma C. Bland[1,2], **Erkka Heino**[2,3], **Michael J. Kosch**[4,5,6], **and Noora Partamies**[1,2]

[1]Birkeland Centre for Space Science, Bergen, Norway, [2]Department of Arctic Geophysics, University Centre in Svalbard, Longyearbyen, Norway, [3]Department of Physics and Technology, University of Tromsø, Tromsø, Norway, [4]Physics Department, Lancaster University, Lancaster, UK, [5]South African National Space Agency, Hermanus, South Africa, [6]Department of Physics and Astronomy, University of Western Cape, Bellville, South Africa

Abstract Two solar proton events in September 2017 had a significant impact on the operation of the Super Dual Auroral Radar Network (SuperDARN), a global network of high-frequency (HF) radars designed for observing *F* region ionospheric plasma convection. Strong polar cap absorption caused near-total loss of radar backscatter, which prevented the primary SuperDARN data products from being determined for a period of several days. During this interval, the high-latitude and polar cap radars measured unusually low levels of background atmospheric radio noise. We demonstrate that these background noise measurements can be used to observe the spatial and temporal evolution of the polar cap absorption region, using an approach similar to riometry. We find that the temporal evolution of the SuperDARN radar-derived HF attenuation closely follows that of the cosmic noise absorption measured by a riometer. Attenuation of the atmospheric noise up to 10 dB at 12 MHz is measured within the northern polar cap, and up to 14 dB in the southern polar cap, which is consistent with the observed backscatter loss. Additionally, periods of enhanced attenuation lasting 2–4 hr are detected by the midlatitude radars in response to M- and X-class solar flares. Our results demonstrate that SuperDARN's routine measurements of atmospheric radio noise can be used to monitor 8- to 20-MHz radio attenuation from middle to polar latitudes, which may be used to supplement riometer data and also to investigate the causes of SuperDARN backscatter loss during space weather events.

Plain Language Summary Solar proton events are known to cause widespread disruption to high-frequency (HF) radio communications in the high-latitude and polar regions. We demonstrate that SuperDARN HF radars may be used to monitor HF radio wave attenuation during solar proton events using routine measurements of the background radio noise. These background noise measurements are produced as part of the radar data processing, but they are not normally used for science applications. We focus on two solar proton events, which occurred in September 2017, and find that the measured radio attenuation is confined to the polar cap and exhibits temporal and spatial properties that are characteristic of polar cap absorption events. The attenuation measured by the Rankin Inlet SuperDARN radar agrees well with measurements from a nearby riometer, indicating that reasonable estimates of the HF radio attenuation can be obtained from SuperDARN radars despite the high day-to-day variability of the atmospheric radio noise. Our technique may also prove useful for determining the reasons for backscatter loss, particularly when riometer data are not available.

Key Points:
- SuperDARN HF radars were strongly affected by polar cap absorption events in September 2017
- A novel method to estimate HF attenuation using SuperDARN atmospheric noise measurements has been developed
- Up to 14-dB attenuation at 12 MHz was measured in the polar caps, resulting in backscatter loss

Correspondence to:
E. C. Bland,
emmab@unis.no

Citation:
Bland, E. C., Heino, E., Kosch, M. J., & Partamies, N. (2018). SuperDARN radar-derived HF radio attenuation during the September 2017 solar proton events. *Space Weather*, *16*, 1455–1469. https://doi.org/10.1029/2018SW001916

Received 24 APR 2018
Accepted 3 AUG 2018
Accepted article online 10 AUG 2018
Published online 2 OCT 2018

1. Introduction

Ionospheric disturbances caused by solar flares and solar energetic particles are known to disrupt high-frequency (HF, 3–30 MHz) transionospheric radio systems, including HF communication systems used in aviation, maritime, and emergency management, as well as over-the-horizon radars used in applications such as ionospheric research, coastal hazard management, and defense (e.g., Ferguson et al., 2015; Goodman, 2005; Knipp et al., 2016). These ionospheric disturbances cause electron density enhancements which affect HF radio propagation in two distinct ways: (1) increased radio wave attenuation in the *D* region ionosphere (50–90 km) due to collisions between electrons and neutral particles, and (2) changes to the available ionospheric propagation paths in the *E* region (90–150 km) and *F* region (150–600 km). Electron density enhancements in the *D* region arise due to energetic proton precipitation and photoionization from soft X-ray

radiation, whereas enhancements in the *E* and *F* regions arise primarily from extreme ultraviolet and soft X-ray radiation. At auroral latitudes, energetic electron precipitation is also a significant source of ionization above ~100-km altitude. This study focuses on the effects of *D* region electron density enhancements caused by solar proton events (SPEs) and their associated solar flares.

A solar proton event is characterized by the increased flux of high-energy (>10 MeV) protons from the Sun. Solar protons impact the Earth's atmosphere in the polar regions causing increased ionization of the *D* region ionosphere. The size of the affected region depends on the particle rigidity (momentum per unit charge) and the shape of the geomagnetic field, and typically extends from about 60° to 90° geomagnetic latitude (Kress et al., 2010). Consequently, the associated radio absorption is termed *polar cap absorption* (PCA) (Bailey, 1964). PCA is most pronounced in the sunlit ionosphere where the effective recombination coefficient below 80-km altitude is lower (e.g., Hargreaves et al., 1993; Ranta et al., 1995). Since PCA events may last for several days, they have significant consequences for high-latitude users of HF communications, such as commercial airlines operating on transpolar routes (Jones et al., 2005).

The particle acceleration for SPEs is driven by solar flare and/or coronal mass ejection processes (Kallenrode, 2003; Reames, 1999). A solar flare is a brief, explosive release of broadband electromagnetic radiation from the solar surface lasting from minutes to hours. Extreme ultraviolet and X-ray radiation released during the flare may cause excess ionization of the lower dayside ionosphere, resulting in brief periods of strong HF radio absorption known as shortwave fadeout (SWF). SWF affects only those communications circuits that have an ionospheric reflection point in the sunlit ionosphere, since the nightside of the Earth is shielded from the X-ray radiation.

PCA and SWF have been studied for several decades using riometers (e.g., Brodrick et al., 2005; Fiori & Danskin, 2016; Kavanagh et al., 2004; Reid & Leinbach, 1959, 1961), as well as incoherent scatter radars (e.g., Hargreaves et al., 1987; Mendillo & Evans, 1974), very low frequency (VLF) receivers (e.g., Kossey et al., 1983; Wenzel et al., 2016), and Global Positioning System satellite measurements of total electron content (Garcia-Rigo et al., 2007). Recently, there have been efforts to utilize existing HF radio infrastructure to monitor the ionospheric effects of space weather events, in particular, SWF. For example, Frissell et al. (2014) demonstrated that data sent to amateur radio reporting networks can be used to identify communications circuits affected by SWF. Also, several studies have demonstrated that the Super Dual Auroral Radar Network (SuperDARN) may be used to detect SWF at midlatitudes. In this case, the HF radio waves transmitted by the radars are absorbed by the *D* region, resulting in the loss of radar backscatter (Chakraborty et al., 2018; Watanabe & Nishitani, 2013). Also, the background radio noise levels measured by each radar decrease sharply at the event onset and gradually recover to nominal levels in the hours following the flare (Berngardt et al., 2018). In this study we build upon this work to demonstrate that SuperDARN radars may also be used to monitor the spatial and temporal evolution of PCA. In particular, we utilize the background noise measurements from SuperDARN radars to quantify the degree of attenuation using an approach similar to riometry. We demonstrate this capability through case studies of two solar proton events which occurred in September 2017.

2. Instrumentation

2.1. The SuperDARN

The primary instruments used in this study are the SuperDARN HF radars. SuperDARN is a global network of high-frequency (HF) radars designed for studying large-scale ionospheric plasma convection from middle to polar latitudes (Chisham et al., 2007; Greenwald et al., 1995; Lester, 2013). As of 2018 the network consists of 23 radars in the Northern Hemisphere and 12 radars in the Southern Hemisphere. The radars detect coherent backscatter from field-aligned electron density irregularities, which are used as tracers for measuring the *F* region plasma convection. The radars may also detect backscatter from the ground/sea and from meteor plasma trails at around 90-km altitude. When a scattering target is detected, the power (signal-to-noise ratio), Doppler velocity, and spectral width of the received backscatter are determined. These parameters are used for studying the ionospheric signatures of a wide range of phenomena, including the structure and dynamics of global convection (e.g., Ruohoniemi & Baker, 1998), polar cap expansion during substorms (e.g., Bristow & Jensen, 2007), ultralow frequency magnetohydrodynamic waves (e.g., Ponomarenko et al., 2003), and gravity waves (e.g., Bristow et al., 1996). A range of methods have also been developed for determining ionospheric critical frequencies and electron densities using SuperDARN radars (Bland et al., 2014; Gillies et al., 2009, 2011;

Figure 1. (top panel) Locations and fields of view of the Clyde River (CLY), Rankin Inlet (RKN), Saskatoon (SAS), and Christmas Valley East (CVE) SuperDARN radars. The location of the riometer at Taloyoak (TALO) is shown in red. (bottom panel) Locations and fields of view of the South Pole Station (SPS), McMurdo Sound (MCM), Dome C East (DCE), and Zhongshan (ZHO) SuperDARN radars. The blue shading shows the position of the beam used in Figures 2 and 7. Dotted and dashed lines show geographic and geomagnetic coordinates, respectively.

Hughes et al., 2002; Ponomarenko et al., 2011; Sarno-Smith et al., 2016), in some cases taking advantage of the real-time availability of data from some radars.

Each SuperDARN radar consists of a linear array of log-periodic or twin-terminated folded dipole antennas, which are phased electronically to produce a narrow (~3.24°), steerable beam. For most radars, this beam can be steered in 16 different azimuthal directions (numbered 0–15), while some newer radars in the network operate with up to 24 azimuthal beams and thus have wider fields of view. The fields of view of four SuperDARN radars in North America and another four in Antarctica are shown in Figure 1, with one beam shaded for each radar. The antennas exhibit significant gain from approximately 10° to 45° in vertical elevation (e.g., Milan et al., 1997), so the beam is narrow in azimuth but wide in vertical elevation.

SuperDARN radars are designed to operate in the frequency range of 8–20 MHz; however, in practice, most radars operate in the 10–15-MHz range. The radars employ a multipulse sequence method (Greenwald et al., 1985; Ribeiro et al., 2013), which allows all of the radar's range gates to be sampled together in each scan. In the standard mode of operation, called *common mode*, the beams are sampled sequentially with a ~3 s or ~7 s

dwell time. It therefore takes either 1 or 2 minutes to scan all beams in the field of view, which sets the time resolution of the data products. The standard range gate resolution is 45 km.

The primary data products of SuperDARN (power, Doppler velocity, and spectral width) are determined using a fitting routine in the SuperDARN data analysis software called FITACF. FITACF also estimates the background noise level (called the *sky noise* in the data files), which is used to determine which range gates contain coherent backscatter. This background noise measurement is the focus of this study. The noise level is estimated as the average of the 10 lowest values of the lag zero power recorded in all of the radar's range gates (there are between 70 and 110 range gates depending on the radar's configuration). In a recent upgrade to the software, a correction for the effective number of noise samples is also applied, without which the noise level would be underestimated. This method is appropriate for SuperDARN radars because the available ionospheric propagation modes (half-hop, one-hop, etc.) confines the observed backscatter to particular bands of range gates. In this study we have processed the raw radar data using this updated version of FITACF (FITACF 3.0, https://doi.org/10.5281/zenodo.1143675), which uses the condition SNR $\geq$ 1 to identify coherent backscatter. We emphasize that the background noise parameter is available for every scan, including intervals when no coherent backscatter was detected in any range gate. Thus, the noise measurement is available during strong PCA events when the power, velocity, and spectral width parameters cannot be measured.

2.2. Supporting Instrumentation

In this study we also use data from the GO Canada 30 MHz single-beam riometer located at Taloyoak (69.54°N, 93.56°W; Rostoker et al., 1995). A riometer (relative ionospheric opacity meter) is a passive instrument consisting of a radio receiver operating in the 20- to 60-MHz frequency range (Little & Leinbach, 1959). The background radio spectrum at these frequencies is dominated by cosmic radio noise. A reduction in the cosmic radio noise measured at ground level may be attributed to attenuation by the ionosphere and is called *cosmic noise absorption* (CNA). CNA is measured relative to a *quiet day curve* (QDC), which is the background noise level during undisturbed ionospheric conditions and is a function of sidereal time. The QDCs are derived using historical data from the riometer; the method used to baseline the GO Canada riometer data is described in http://aurora.phys.ucalgary.ca/norstar/rio/doc/CANOPUS_Riometer_Baselining.pdf.

We also use integral particle flux measurements from one of the Geosynchronous Operational Environmental Satellites (GOES) (NASA, 2006), which is operated by the National Oceanic and Atmospheric Administration (NOAA). We use the particle flux data from the GOES-15 spacecraft, which is positioned in geosynchronous orbit at 135.0°W. The integral particle flux data are measured by the GOES-15 energetic particle sensor and are provided for energy ranges $\geq$10 MeV, $\geq$50 MeV, and $\geq$100 MeV at 5 min time resolution.

3. SuperDARN Response to the Solar Proton Events

The two solar proton events considered in this study occurred in September 2017. These two events were identified using a standard definition based on proton flux measurements from NOAA-GOES spacecraft — the start of the event is the first of three consecutive measurements of >10-MeV protons with fluxes greater than 10 $cm^{-2}{\cdot}sr^{-1}{\cdot}s^{-1}$, and the event ends when the flux exceeds this value for the last time (https://umbra.nascom.nasa.gov/SEP/). The first panel of Figure 2 shows the integral proton flux measured by the GOES-15 satellite from 1 to 16 September 2017. The two SPEs are labeled as *Event 1* and *Event 2*. Based on the above event threshold level (indicated by the horizontal dashed line in the figure), Event 1 commenced at 01:25 UT on 5 September and ended at 22:45 UT on 8 September. Event 2 commenced at 16:45 UT on 9 September and ended at 17:10 UT on 14 September.

We will first consider the response of four North American SuperDARN radars to the SPEs. The top panel of Figure 1 shows the locations and fields of view of the Clyde River (CLY), Rankin Inlet (RKN), Saskatoon (SAS), and Christmas Valley East (CVE) radars. The blue shading shows the position of beam 5 for the CLY radar and beam 7 for the other three radars. These beams were chosen because they are near the center of each radar's field of view and had continuous temporal coverage for the time period shown. The response of these four radars to the SPEs is shown in the second–fifth panels of Figure 2. The red line in each panel shows the instantaneous echo occurrence, which is the percentage of range gates containing coherent backscatter for a single scan. Prior to the onset of Event 1, the instantaneous echo occurrence at each site ranges from approximately 5% to 40%. During Event 1, the echo occurrence for the two polar cap radars (CLY and RKN) approaches zero when the radars are positioned on the dayside of the Earth. This occurs at CLY from ~09:30 to 23:30 UT, and at RKN

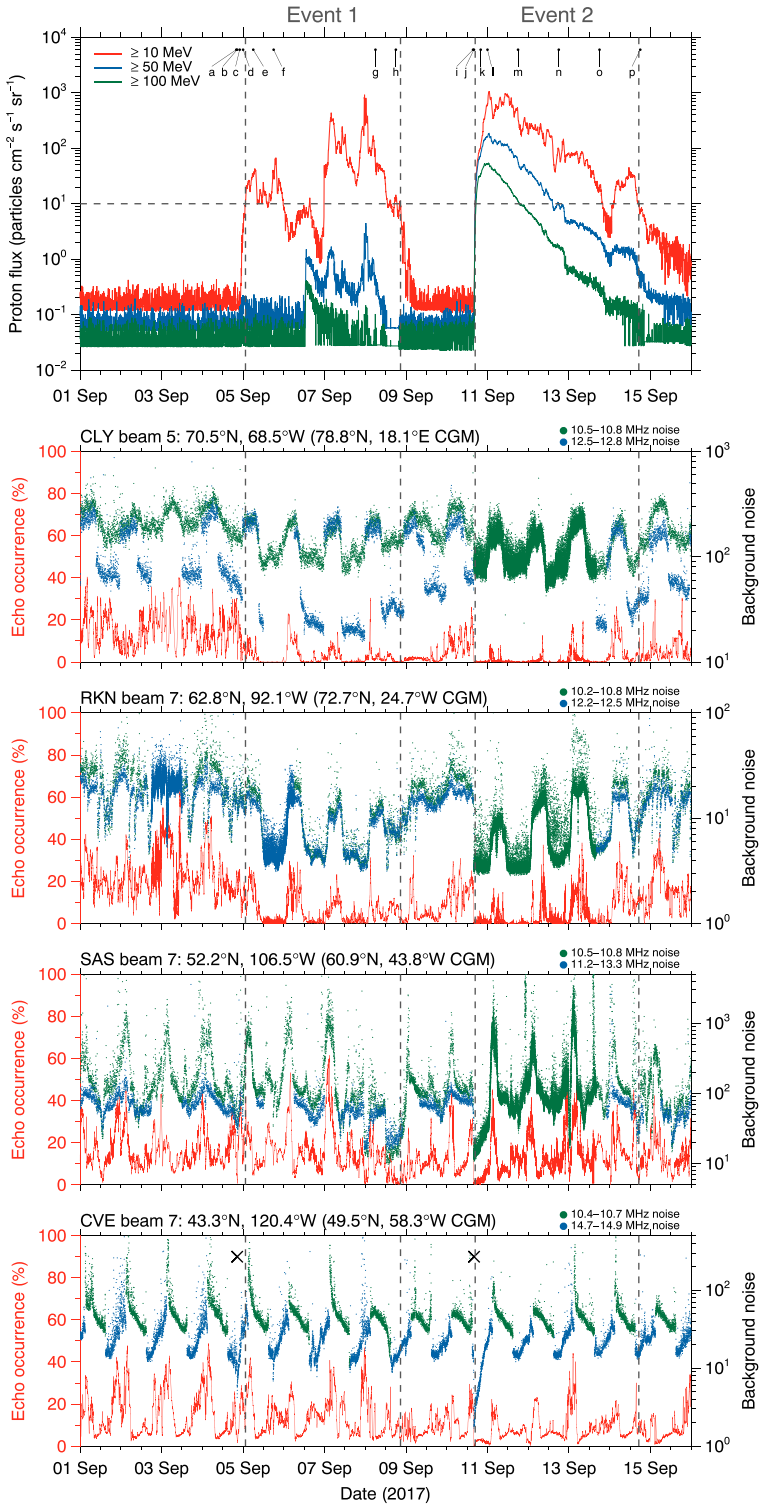

Figure 2. (first panel) Proton fluxes measured by the NOAA GOES-15 satellite from 1 to 16 September 2017. Echo occurrence (red) and background noise measurements (blue and green) from the (second panel) Clyde River (CLY), (third panel) Rankin Inlet (RKN), (fourth panel) Saskatoon (SAS), and (fifth panel) Christmas Valley East (CVE) SuperDARN radars. Solar noon at these stations occurs at approximately 16:31 UT (CLY), 18:05 UT (RKN), 19:03 UT (SAS), and 19:59 UT (CVE). The vertical dashed lines indicate the start and end times of the two solar proton events labeled *Event 1* and *Event 2*, and the black crosses in the fifth panel show the onset time of two solar X-ray flares. The letters (a)–(p) in the first panel correspond to times shown in Figure 6. NOAA = National Oceanic and Atmospheric Administration; GOES = Geostationary Operational Environmental Satellite; SuperDARN = Super Dual Auroral Radar Network.

from ~11:30 to 00:30 UT. The echo occurrence recovers briefly from 10 to 11 September, up until the onset of Event 2 when the dayside echo occurrence nears zero again. During Event 2, very little backscatter was detected by the CLY radar at any local time. At Rankin Inlet, located several degrees equatorward of Clyde River, backscatter was detected only during the night (~00:30–11:30 UT). The low echo occurrence indicates that the radio waves transmitted by the CLY and RKN radars were strongly attenuated by the ionosphere during the periods of enhanced proton flux. This effect is most pronounced during the daytime, which is expected for PCA events (see section 1).

At Saskatoon, the echo occurrence approaches zero toward the end of Event 1 and also near the beginning of Event 2. This approximately coincides with the increased flux of higher-energy protons (≥50 MeV). Similarly, the echo occurrence at Christmas Valley East decreased slightly toward the end of Event 1 and more significantly during Event 2. Due to the low latitude of the CVE radar, the data set is dominated by ground backscatter, which produces the regular daytime occurrence peaks in Figure 2 from 1 to 5 September (~13:30–02:20 UT). Thus, the reduction or absence of these peaks is evidence of enhanced attenuation by the *D* region on the dayside.

The blue and green symbols in Figure 2 show the background noise measured by each radar. The color coding indicates the frequency at which the noise was measured. For most of the time interval shown, CLY, RKN, and SAS were alternating between two frequency bands, and CVE alternated between a daytime and nighttime frequency every 12 hr. The use of different frequency bands produces the discontinuities in the noise measurements, with higher frequencies associated with lower noise levels. During both SPEs, there is a decline in the overall noise level at CLY and RKN, indicating that the background radio noise was attenuated during the SPEs. This is particularly apparent for the 12.5- to 12.8-MHz data at CLY during Event 1 for which the daytime (~09:30–23:30 UT) noise level is reduced by a factor of ~3.

The background noise behaves differently at Saskatoon and Christmas Valley East compared to the polar cap. For these radars, there is a sharp decrease in the noise level and the instantaneous echo occurrence just prior to each SPE. This behavior coincides with the release of two solar flares, which are marked by the crosses in the fifth panel of Figure 2. For the flare on 4 September, the sudden decrease in the noise level observed at SAS and CVE and the gradual recovery to preflare levels over a 1- to 2-hr period agrees well with SuperDARN observations of SWF by Berngardt et al. (2018). There is also a sudden decrease in the noise levels at SAS and CVE following the flare on 10 September. In this case the recovery time at both radar sites is about 10 hr. This longer recovery time may be due to strong *D* region ionization at midlatitudes caused by the increased flux of ≥100-MeV protons near the beginning of Event 2. This makes it difficult to distinguish between the ionospheric disturbance caused by the solar flare and the disturbance due to the solar protons.

The results presented in Figure 2 indicate that both the SuperDARN echo occurrence and the background sky noise parameters respond to the enhanced particle flux associated with solar proton events. These data can be used to observe the spatial and temporal evolution of PCA caused by solar energetic particles. In section 5 we will use the SuperDARN background noise measurements to quantify the degree of attenuation during the September 2017 solar proton events using methods derived from riometry. To perform this estimate, it is first necessary to characterize the behavior of the noise in the absence of any ionospheric disturbances.

4. SuperDARN Background Noise

A key difference between riometers and SuperDARN radars is that the radio spectrum at their respective operating frequencies arise from different sources. At riometer operating frequencies (20–60 MHz), the background radio spectrum is dominated by cosmic radio noise. For an undisturbed ionosphere, the cosmic noise at a given frequency varies with sidereal time only. In contrast, at the typical SuperDARN operating frequencies (10–15 MHz), the radio spectrum is dominated by atmospheric noise, which arises primarily from lightning strikes (Headrick & Anderson, 2008). Although lightning strikes occur most frequently in the tropics, their radio emissions can propagate to polar latitudes via the ionosphere. Therefore, the atmospheric noise measured by SuperDARN radars from middle to polar latitudes is controlled by both the global distribution of thunderstorm activity and the ionospheric propagation conditions (e.g., Giordano & Haber, 1972). In contrast to cosmic noise, atmospheric noise is mostly a function of *solar time* and exhibits day-to-day and seasonal variability.

Background noise measurements from the Zhongshan SuperDARN radar for the year 2012 are shown in the top panel of Figure 3. This radar is located in the southern polar cap at 69.38°S, 76.38°E (74.9°S, 97.2°E geomagnetic), as shown in the lower panel of Figure 1. We have chosen the Zhongshan radar to illustrate the

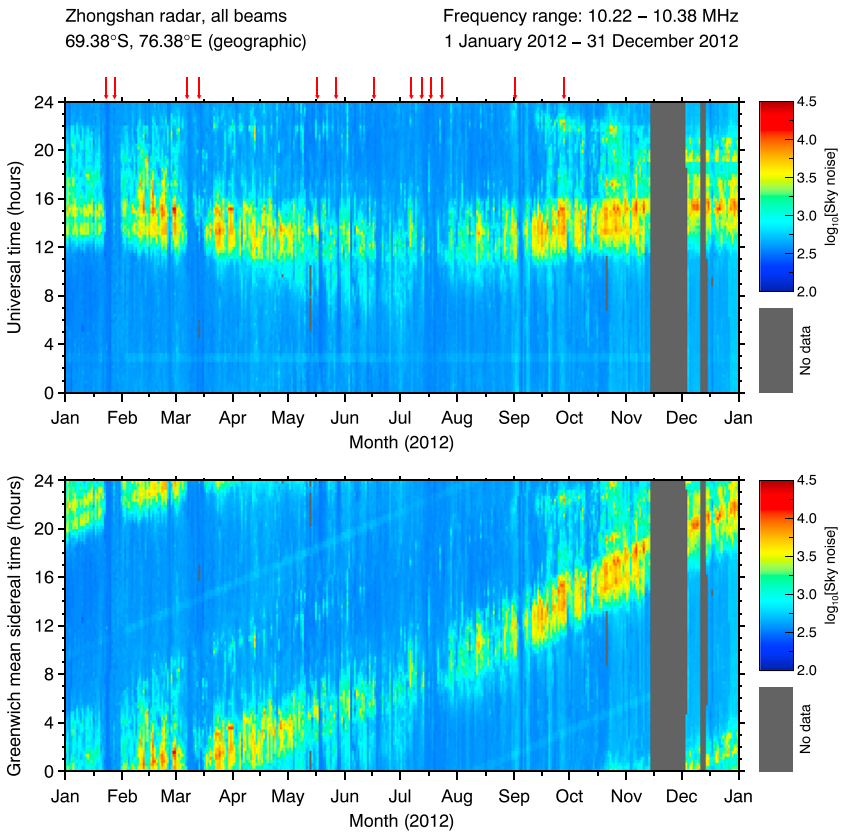

Figure 3. Background noise for the year 2012 measured by the Zhongshan SuperDARN radar. In the top (bottom) panel, the diurnal variation is plotted as a function of universal time (sidereal time). The red arrows indicate the onset times of solar proton events. SuperDARN = Super Dual Auroral Radar Network.

behavior of SuperDARN noise measurements because this radar operated in a fixed, narrow frequency band (10.22–10.38 MHz) for the entire year. This makes it straightforward to visualize the diurnal and seasonal variation of the noise, as well as the effects of multiple SPEs which occurred in 2012. The noise data have been binned according to universal time and day of year. The noise exhibits a clear diurnal trend, with a daily maximum at around 13:00–15:00 UT, which corresponds to 18:00–20:00 local time at the radar site. Lower noise levels were measured in the Antarctic winter months (June, July, August), which is expected due to the reduced lightning activity and lower ionospheric electron densities in the winter hemisphere. The red arrows on the top horizontal axis indicate the onset times for the 13 SPEs which occurred in 2012. There is a decrease in the noise level for each SPE lasting for several days, which we attribute to polar cap absorption.

The bottom panel of Figure 3 shows the same data set binned according to Greenwich mean sidereal time instead of universal time. Any significant sidereal-time-dependent component in the SuperDARN sky noise would manifest itself in this plot as an approximately horizontal feature. However, no such feature is apparent. Therefore, we conclude that the SuperDARN sky noise parameter is controlled by terrestrial sources, namely. atmospheric noise. This result will be used in the next section to generate 'quiet day curves' for SuperDARN radars.

5. SuperDARN Radar-Derived HF Attenuation

To estimate the radio attenuation at each radar site, we have adopted a procedure similar to the methods used for determining CNA from riometer data. The first step is to construct QDCs for the SuperDARN data, analogous to riometer QDCs. For this purpose we have used the SuperDARN data set spanning the interval 1–31 August 2017. Since the background noise is frequency dependent (see Figure 2), we separated the data from each radar into frequency bands. Throughout August and September 2017, most radars operated in two distinct frequency bands, either alternating between the two bands every minute or operating in one frequency band during the day and a different band at night. Brief periods in which the radars were operated

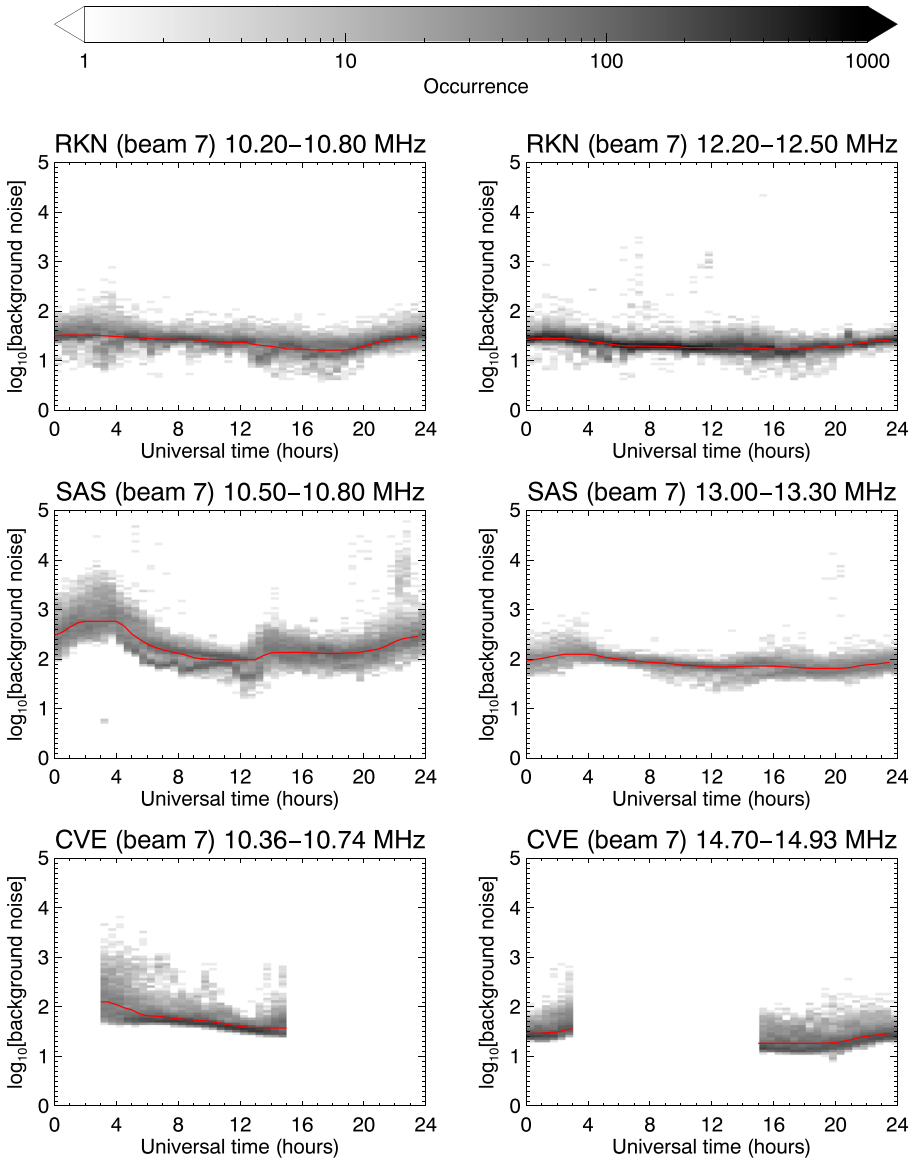

Figure 4. Two-dimensional histograms of the background *sky* noise measured by the Rankin Inlet (RKN), Saskatoon (SAS), and Christmas Valley East (CVE) radars (beam 7 only). The red lines show the final quiet day curves after smoothing.

at other frequencies were excluded. Time intervals for which the radars were operated with a range resolution other than 45 km were also excluded, since we have observed that the noise level changes when the range gate resolution is changed (not shown). The remaining data set covered a minimum of 25 days in August for each radar.

We have observed that the background noise level varies with the azimuthal beam direction, particularly near the solar terminator for the eastward and westward oriented beams. Therefore, separate QDCs were generated for each radar beam and also for each frequency band. The noise measurements for August 2017 were binned into 30-min intervals of universal time (UT), and the median value of the noise in each UT bin was determined. The resulting curve was then smoothed by median filtering to obtain the final QDC. This procedure is illustrated in Figure 4 for beams 7 of the RKN, SAS, and CVE radars. The color scale shows the noise distribution in universal time from 1 to 31 August 2017, and the red lines show the smoothed median noise levels which are used as the QDCs. The gaps in the CVE data arise because the radar operated in separate daytime and nighttime frequency bands. Using median atmospheric noise measurements to produce the QDCs should automatically exclude the effects of any short-term ionospheric disturbances such as SWF in the

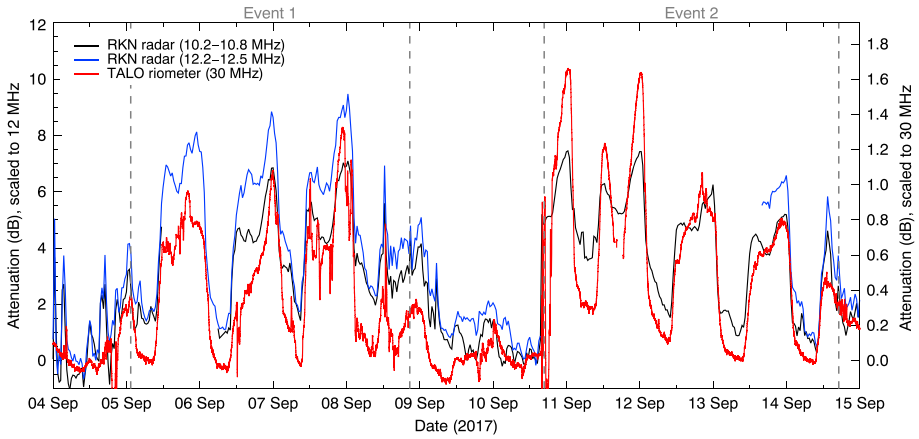

Figure 5. Radio attenuation measured by the Rankin Inlet SuperDARN radar (RKN) and the 30-MHz cosmic noise absorption measured by the Taloyoak riometer (TALO). The radar- and riometer-derived attenuation values can be read using both vertical axes, which show the equivalent attenuation at 12 MHz and 30 MHz. The vertical dashed lines indicate the start and end times of the two solar proton events labeled *Event 1* and *Event 2*.

QDC data set. Long-duration disturbances caused by SPEs or intense geomagnetic storms would affect the accuracy of the QDCs and should be excluded; however, no such events occurred during August 2017.

Following standard methods used in riometry (e.g., Brodrick et al., 2005; Rosenberg et al., 1991), the attenuation relative to the QDC was then determined for each beam and frequency band as

$$A = 10 \log_{10} \left[\frac{N_{\mathrm{QDC}}}{N} \right] \tag{1}$$

where N is the measured background noise and N_{QDC} is the value of the quiet day curve at the corresponding universal time.

In order to compare attenuation measurements from different frequency bands, and also with CNA measurements from riometers, it is necessary to scale all attenuation measurements to their equivalent values at a common frequency. For HF radio waves, *D* region nondeviative absorption varies as the inverse square of the frequency (e.g., Davies, 1990):

$$A_f = A_0 \left(\frac{f_0}{f} \right)^2 \tag{2}$$

where A_0 is the radio wave attenuation measured at frequency f_0, and A_f is the equivalent attenuation at another frequency f. In this study we have chosen to scale all SuperDARN-derived attenuation values to 12 MHz and also to 30 MHz for comparison with riometer data.

Figure 5 shows the HF attenuation measured on beam 7 of the Rankin Inlet radar from 4 to 15 September 2017. The black (blue) line shows the attenuation measured in the 10.20–10.80 MHz (12.20–12.50 MHz) frequency band. The red line shows the cosmic noise absorption measured by the Taloyoak riometer (TALO). The radar- and riometer-derived attenuation values can be read using both vertical axes; the left axis indicates the equivalent attenuation at 12 MHz, and the right axis indicates the equivalent attenuation at 30 MHz (determined using equation (2).

The temporal evolution of the SuperDARN radar-derived attenuation closely follows the CNA measured by the riometer. The differences between the two data sets may be due to the different methods used to determine the QDCs, and the high day-to-day variability of the atmospheric radio noise which limits the precision of the SuperDARN QDCs (see section 6). Despite these differences, the radar-derived attenuation reproduces the key features of the riometer-derived CNA, specifically the diurnal variation and the shape of the amplitude envelope for both events. This indicates that the QDCs generated from the SuperDARN atmospheric noise measurements provided a reasonable reference noise level from which to estimate the attenuation.

Maps of the SuperDARN radar-derived attenuation for all Northern Hemisphere SuperDARN radars are shown in Figure 6. Each azimuthal beam has been projected out to 900 km from each radar site at 90-km altitude.

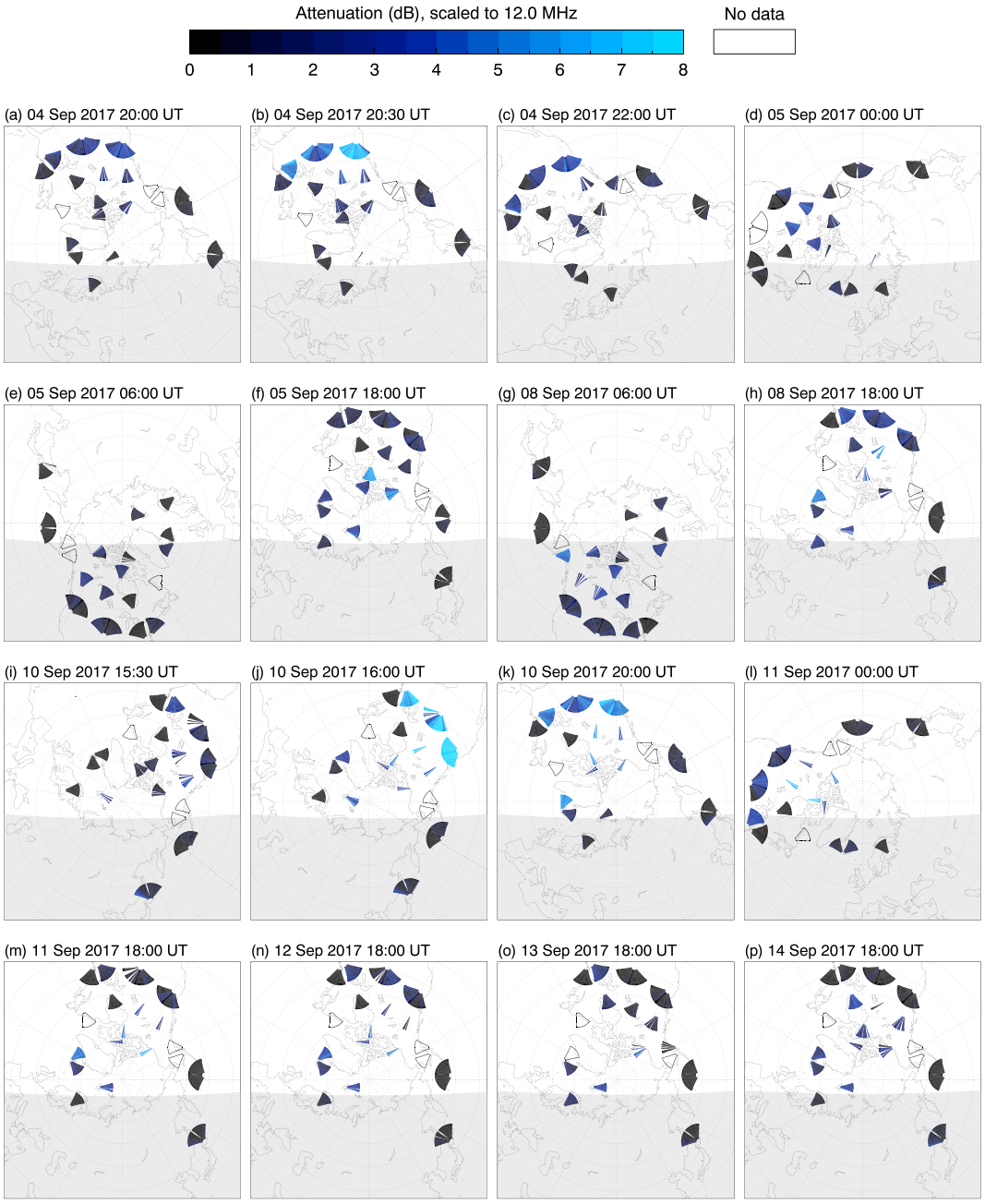

Figure 6. Maps of radio attenuation scaled to 12 MHz for selected time intervals during the two solar proton events. Panels (a)–(d) show the response to the first solar flare on 4 September (20:33 UT). Panels (e)–(h) show the polar cap absorption during Event 1. Panels (i)–(l) show the response to the second solar flare on 10 September (16:06 UT). Panels (m)–(p) show the polar cap absorption during Event 2.

This projection distance is arbitrary because the noise represents the overall background noise level along the beam and cannot be assigned to a specific point in the ionosphere (see section 6). All attenuation values have been scaled to the equivalent attenuation at 12 MHz using equation (2). When the attenuation was measured at two frequencies on a given radar beam, the results were averaged together after scaling. The gray shading in each panel indicates the nightside of the ionosphere. For several of the intervals shown, data from some radars were available only for selected beams, reflecting the use of operational modes other than the common mode. The times shown in panels (a)–(p) correspond to the letters (a)–(p) in the top panel of Figure 2.

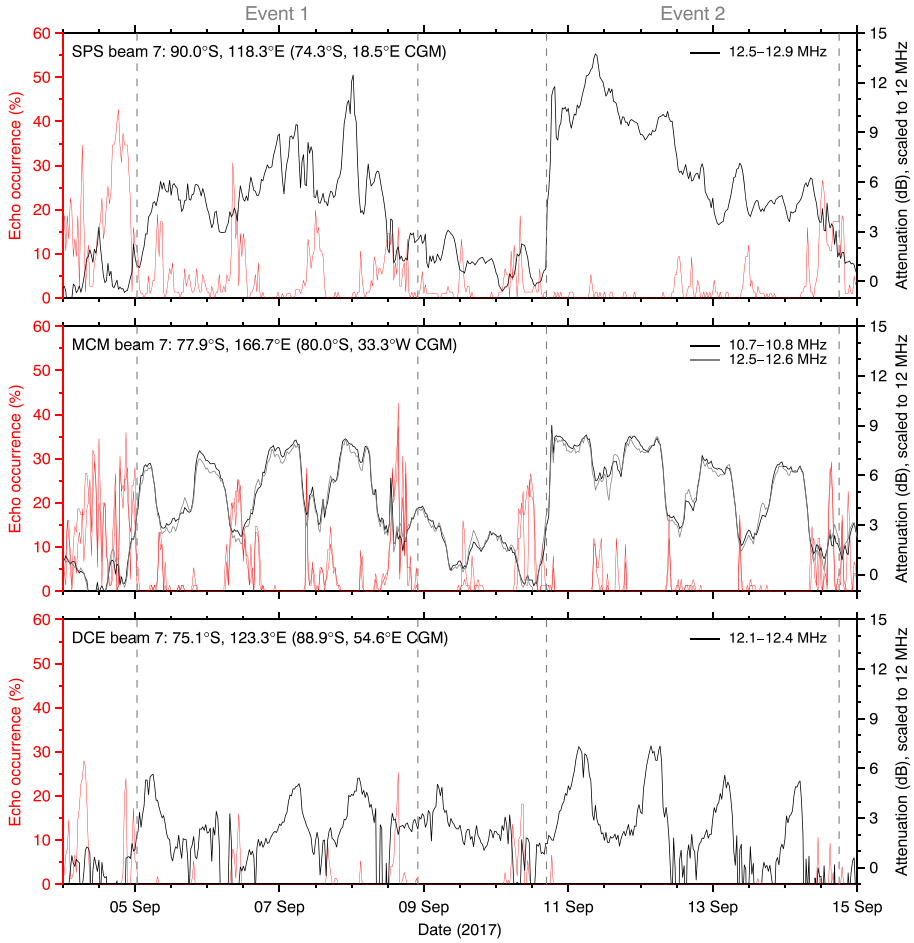

Figure 7. Echo occurrence and radio attenuation measured by the (top) South Pole Station (SPS), (middle) McMurdo Sound (MCM), and (bottom) Dome C East (DCE) SuperDARN radars. The attenuation values have been scaled to 12 MHz using equation (2). Solar noon at MCM and DCE occur at approximately 00:50 UT and 03:43 UT, respectively. CGM=corrected geomagnetic.

Panels (a)–(d) show the midlatitude radar response to the M5 solar flare which occurred at 20:33 UT on 4 September. Prior to the solar flare (panel a), very low levels of attenuation were observed by all radars. A peak in the attenuation occurs at midlatitudes when the flare occurs (panel b), which gradually decays in the hours following the flare (panels c–d).

The evolution of the PCA during Event 1 is shown in panels (e)–(h). Significant attenuation is observed only by the high-latitude and polar cap radars, and thus, the *D* region enhancement associated with the SPE is confined to the polar caps as expected. The radar response to an X8 solar flare at 16:06 UT on 10 September is shown in panels (i)–(l). The response is similar to the M5 flare, with a sudden peak in the midlatitude attenuation which then declines over the following hours. Finally, panels (m)–(p) show the attenuation at 18:00 UT for each day of Event 2. The enhanced attenuation is confined to polar latitudes and decreases gradually as the proton flux decreases.

The HF attenuation during the two SPEs was also determined for three SuperDARN radars located within the southern polar cap — South Pole Station (SPS), McMurdo Sound (MCM), and Dome C East (DCE). The locations and fields of view of these radars are shown in the bottom panel of Figure 1, with beam 7 shaded for each radar. Figure 7 shows the echo occurrence and the attenuation measured on beam 7 for each of these radars, scaled to 12 MHz. All three radars exhibit backscatter loss during the two events. At SPS and MCM, the backscatter loss occurs only at certain local times, whereas at DCE the backscatter loss lasts for almost the entire event.

In addition to the backscatter loss, the SPS, MCM, and DCE radars measure enhanced levels of attenuation during the SPEs, with stronger attenuation occurring at higher geographic latitudes. The attenuation

measured by these radars exhibits similar behavior to the attenuation measured at Rankin Inlet (Figure 5), with the attenuation peaks centered approximately around local midday in each case. At McMurdo Sound, the daytime attenuation maxima coincide with the echo occurrence minima. Similarly, at South Pole Station, backscatter is detected during the SPEs only when the attenuation is low ($\lesssim$4 dB at 12 MHz). These results provide strong evidence that the observed backscatter loss at each radar site is caused by attenuation of the transmitted radio waves, rather than an absence of scattering targets, for example.

6. Discussion

In this paper we have demonstrated that SuperDARN radars can be used to observe the spatial and temporal evolution of polar cap absorption using routine measurements of the background radio noise. This background noise measurement is required for processing the raw radar data and is recorded in the SuperDARN data files, but it is not normally used in science applications. The authors are aware of two previous studies utilizing the background noise data: (1) Berngardt et al. (2018), who showed that background noise measurements by the midlatitude SuperDARN radars can be used to detect shortwave fadeout, and (2) Ponomarenko et al. (2016), who investigated the effect of background noise on long-term echo occurrence rates. These two studies, and our study, highlight the utility of SuperDARN background noise data for monitoring ionospheric disturbances.

Although this study has focused on attenuation due to solar proton events and solar flares, it may also be possible to use SuperDARN radars to detect attenuation caused by other ionospheric disturbances, particularly energetic electron precipitation (EEP) during geomagnetic storms, substorms, and pulsating aurora. The SuperDARN data set consists of more than 20 years of continuous observations, including background noise measurements and may provide a useful addition to riometer, incoherent scatter radar, and optical observations of EEP. Ionospheric disturbances due to EEP are generally weaker than those caused by SPEs and solar flares and would be more difficult to detect within the highly variable atmospheric noise.

The SuperDARN noise measurements may be useful for identifying the causes of SuperDARN backscatter loss. Backscatter loss has been shown to occur for several reasons, including signal attenuation (Milan et al., 1999, 2008), disturbed propagation conditions in the *E* or *F* region (Baker et al., 2007; Currie et al., 2016; Danskin et al., 2002; Gauld et al., 2002), and the suppression of ionospheric irregularities in the observation region (Baker et al., 2007; Milan et al., 1999). Colocated riometer and SuperDARN data are rarely available, so the SuperDARN data may be a substitute for riometer data when determining whether attenuation was the cause of backscatter loss. The *combination* of reduced noise levels and backscatter loss indicates that attenuation has occurred. If backscatter loss results from the absence of scattering targets or disturbed propagation conditions, one would expect no such reduction in the background noise. Backscatter loss may also result from external radio interference, which would be accompanied by an increase in the background noise.

There are several factors that must be considered when interpreting SuperDARN background noise measurements and the HF attenuation values derived from them. First, there is an inherent ambiguity in assigning geographic coordinates to the attenuation values due to the shape of the antenna gain pattern. The gain pattern has a wide vertical extent and oblique orientation, ranging from about 10° to 45° from the horizontal. Furthermore, the antenna gain pattern includes a large backlobe and sidelobes (Milan et al., 1997; Sterne et al., 2011), which are also sensitive to atmospheric noise. Since atmospheric noise is produced equatorward of most SuperDARN radar sites, we anticipate that the backlobe may at times be the dominant contributor to the noise measurement. For example, radars located near the boundary of the PCA region would detect significantly more noise from the equatorward oriented backlobe compared to the poleward oriented main lobe. This makes it difficult to assign geographic coordinates to SuperDARN attenuation measurements.

Further ambiguity arises from the fact that atmospheric noise propagating via the ionosphere to the polar caps traverses the *D* region in at least two separate locations (i.e., for one-hop propagation modes). The radar cannot distinguish between attenuation that occurred close to the radar site and that which occurred ~1,000–2,000 km away where the noise signal propagated from the troposphere to the ionosphere. For PCA events, it is expected that the attenuation is confined to the region poleward of ~60° magnetic latitude, so attenuation measured by the polar cap SuperDARN radars is likely to be caused by an ionospheric enhancement close to the radar site. We can justify this further by considering the absence of radar backscatter during the periods of PCA. Echo returns from polar cap SuperDARN radars are dominated by half-hop ionospheric

backscatter, for which the only *D* region traversal occurs within a few hundred kilometers of the radar site. Therefore, the loss of backscatter from the polar cap radars is evidence that the attenuation occurred close to the radar site.

One should also verify that the SuperDARN-derived attenuation is consistent with the observed backscatter loss. For the two PCA events considered in this work, attenuation up to 10 dB at 12 MHz was detected within the northern polar cap, and up to 14 dB in the southern polar cap. In order for SuperDARN radars to detect ionospheric, ground, or meteor backscatter, the transmitted radio waves traverse the *D* region multiple times and thus undergo significant attenuation when the *D* region is enhanced. Based on the results presented in Figures 5 and 7, which show one-way attenuation, one could reasonably expect 12-MHz waves to undergo a total of 20- to 30-dB attenuation as they propagate to ionospheric scattering targets and back to the radar. Since the SuperDARN backscatter power parameter typically ranges from 0 to 30 dB, this degree of attenuation would extinguish most or all of the backscatter. Therefore, the attenuation values derived from the SuperDARN noise measurements are consistent with the observed backscatter loss.

In Figure 5 we compared the PCA observed by the Rankin Inlet SuperDARN radar and the Taloyoak riometer. Qualitatively, the radar and riometer observations exhibit similar behavior in terms of the dayside (nightside) attenuation maxima (minima), and also the shape of the amplitude envelope. However, there are also some key differences in the two data sets. For example, the RKN radar detects enhanced attenuation on the nightside during Event 1, but the TALO riometer detects no obvious enhancement. Also, the first two dayide attenuation peaks during Event 2 have significantly different amplitudes. We identify several potential contributors to the differences between the radar- and riometer-derived attenuation measurements:

1. the ∼750 km spatial separation between the RKN radar and the TALO riometer;
2. the use of equation (2) to scale the attenuation data to a common frequency;
3. the high variability of the atmospheric noise used for determining the radar attenuation values;
4. differences in the methods used to baseline the radar and riometer data sets (quiet day curve determination).

The spatial separation between the RKN radar and the TALO riometer is unlikely to be a major contributor, because PCA is a large-scale event affecting the entire polar cap. Also, both the radar and the riometer have wide antenna gain patterns, reducing the effect of the station separation. The other factors listed above, however, may be significant. We chose to scale the radar and riometer data to common frequencies using the nondeviative absorption relationship (equation (2) from magnetoionic theory, but empirical relationships also exist in the literature. For example, Sauer and Wilkinson (2008) showed that dayside 10- to 50-MHz PCA varies with frequency as $f^{-1.5}$. Patterson et al. (2001) showed that the frequency exponent is dependent on the particle energy, ranging from −1.2 to −1.8. Other studies have validated the f^{-2} relationship from magnetoionic theory (Rosenberg et al., 1991). For CNA due to solar flares, Schumer (2009) determined an $f^{-1.24}$ relationship. These exponents produce significantly different attenuation values when scaling from 10–15 MHz to 30 MHz. For example, 8-dB attenuation measured at 12 MHz is equivalent to 1.3 dB at 30 MHz using an f^{-2} relationship, or 2.7 dB using an $f^{-1.2}$ relationship. However, there is no single exponent that would account for the differences between the radar and riometer data presented in Figure 5. This is because the TALO riometer consistently measures lower levels of attenuation compared to the RKN radar during Event 1, but for Event 2 the riometer values are, in general, higher than the radar measurements during the day and lower at night.

We suggest that both items (3) and (4) from the above list are responsible for the observed attenuation differences in Figure 5. A variety of methods exist for producing riometer QDCs, and so the particular CNA curve obtained after baselining can vary significantly. Additionally, the high variability of atmospheric noise introduces a source of error into the SuperDARN QDCs that does not apply to riometer QDCs derived from cosmic noise. In particular, it is not possible to distinguish between reduced production of atmospheric noise and increased attenuation based on SuperDARN noise measurements alone. This highlights the importance of considering the instantaneous echo occurrence together with the noise measurements to confirm that attenuation has taken place, since reduced atmospheric noise production would not cause backscatter loss.

7. Conclusion

We have demonstrated that SuperDARN radars can be used to observe the spatial and temporal evolution of 10- to 15-MHz polar cap absorption by utilizing routine background noise measurements. PCA is identified in the SuperDARN data set as a combination of reduced background noise and near-total loss of backscatter

lasting for several days. Following methods used in riometry, we produced QDCs describing the SuperDARN atmospheric noise for undisturbed conditions and estimated the degree of attenuation relative to these QDCs. For our two case study PCA events in September 2017, attenuation up to 10 dB at 12 MHz was detected within the northern polar cap, and up to 14 dB in the southern polar cap. Radar-derived attenuation values from Rankin Inlet agree qualitatively with CNA measurements from the Taloyoak riometer. In addition to the PCA, brief attenuation enhancements lasting 2–4 hr were observed at midlatitudes, consistent with previous SuperDARN observations of shortwave fadeout caused by solar X-ray flares. We emphasize that the SuperDARN noise measurement is available for every scan and can therefore be used to measure HF attenuation even during intervals of backscatter loss when the primary SuperDARN data products cannot be determined.

Acknowledgments
This study was supported by the Research Council of Norway/CoE under contract 223252/F50. The SuperDARN data were obtained from the British Antarctic Survey data mirror (https://www.bas.ac.uk/project/superdarn). SuperDARN is a collection of radars funded by the national scientific funding agencies of Australia, Canada, China, France, Japan, Norway, South Africa, United Kingdom, and United States of America. The GO Canada (previously NORSTAR) riometer array is operated by the University of Calgary with financial support from the Canadian Space Agency. All riometer data are openly available from data.phys.ucalgary.ca. The authors also acknowledge NOAA for the GOES proton flux data (https://www.ngdc.noaa.gov/stp/satellite/goes/dataaccess.html).

References

Bailey, D. K. (1964). Polar-cap absorption. *Planetary and Space Science*, *12*(5), 495–541. https://doi.org/10.1016/0032-0633(64)90040-6

Baker, J. B. H., Greenwald, R. A., Ruohoniemi, J. M., Oksavik, K., Gjerloev, J. W., Paxton, L. J., et al. (2007). Observations of ionospheric convection from the Wallops SuperDARN radar at middle latitudes. *Journal of Geophysical Research*, *112*, A01303. https://doi.org/10.1029/2006JA011982

Berngardt, O. I., Ruohoniemi, J. M., Nishitani, N., Shepherd, S. G., Bristow, W. A., & Miller, E. S. (2018). Attenuation of decameter wavelength sky noise during X-ray solar flares in 2013–2017 based on the observations of midlatitude HF radars. *Journal of Atmospheric and Solar-Terrestrial Physics*, *173*, 1–13. https://doi.org/10.1016/j.jastp.2018.03.022

Bland, E. C., McDonald, A. J., de Larquier, S., & Devlin, J. C. (2014). Determination of ionospheric parameters in real time using SuperDARN HF radars. *Journal of Geophysical Research: Space Physics*, *119*, 5830–5846. https://doi.org/10.1002/2014JA020076

Bristow, W. A., Greenwald, R. A., & Villain, J. P. (1996). On the seasonal dependence of medium-scale atmospheric gravity waves in the upper atmosphere at high latitudes. *Journal of Geophysical Research*, *101*(A7), 15,685–15,699. https://doi.org/10.1029/96JA01010

Bristow, W. A., & Jensen, P. (2007). A superposed epoch study of SuperDARN convection observations during substorms. *Journal of Geophysical Research*, *112*, A06232. https://doi.org/10.1029/2006JA012049

Brodrick, D., Tingay, S., & Wieringa, M. (2005). X-ray magnitude of the 4 November 2003 solar flare inferred from the ionospheric attenuation of the galactic radio background. *Journal of Geophysical Research*, *110*, A09S36. https://doi.org/10.1029/2004JA010960

Chakraborty, S., Ruohoniemi, J. M., Baker, J. B. H., & Nishitani, N. (2018). Characterization of short-wave fadeout seen in daytime SuperDARN ground scatter observations. *Radio Science*, *53*, 472–484. https://doi.org/10.1002/2017RS006488

Chisham, G., Lester, M., Milan, S. E., Freeman, M. P., Bristow, W. A., Grocott, A., et al. (2007). A decade of the Super Dual Auroral Radar Network (SuperDARN): Scientific achievements, new techniques and future directions. *Surveys in Geophysics*, *28*, 33–109. https://doi.org/10.1007/s10712-007-9017-8

Currie, J. L., Waters, C. L., Menk, F. W., Sciffer, M. D., & Bristow, W. A. (2016). SuperDARN backscatter during intense geomagnetic storms. *Radio Science*, *51*(6), 814–825. https://doi.org/10.1002/2016RS005960

Danskin, D. W., Koustov, A. V., Ogawa, T., Nishitani, N., Nozawa, S., Milan, S. E., et al. (2002). On the factors controlling occurrence of *F*-region coherent echoes. *Annales de Geophysicae*, *20*(9), 1385–1397. https://doi.org/10.5194/angeo-20-1385-2002

Davies, K. (1990). *Ionospheric Radio*, no 31 in IEE electromagneitc waves series. London: Peter Peregrinus Ltd.

Ferguson, D. C., Worden, S. P., & Hastings, D. E. (2015). The space weather threat to situational awareness, communications, and positioning systems. *IEEE Transactions on Plasma Science*, *43*(9), 3086–3098. https://doi.org/10.1109/TPS.2015.2412775

Fiori, R., & Danskin, D. (2016). Examination of the relationship between riometer-derived absorption and the integral proton flux in the context of modeling polar cap absorption. *Space Weather*, *14*, 1032–1052. https://doi.org/10.1002/2016SW001461

Frissell, N. A., Miller, E. S., Kaeppler, S. R., Ceglia, F., Pascoe, D., Sinanis, N., et al. (2014). Ionospheric sounding using real-time amateur radio reporting networks. *Space Weather*, *12*, 651–656. https://doi.org/10.1002/2014SW001132

Garcia-Rigo, A., Hernández-Pajares, M., Juan, J. M., & Sanz, J. (2007). Solar flare detection system based on global positioning system data: First results. *Advances in Space Research*, *39*(5), 889–895. https://doi.org/10.1016/j.asr.2006.09.031

Gauld, J. K., Yeoman, T. K., Davies, J. A., Milan, S. E., & Honary, F. (2002). SuperDARN radar HF propagation and absorption response to the substorm expansion phase. *Annales de Geophysicae*, *20*(10), 1631–1645. https://doi.org/10.5194/angeo-20-1631-2002

Gillies, R. G., Hussey, G. C., Sofko, G. J., McWilliams, K. A., Fiori, R. A. D., Ponomarenko, P., et al. (2009). Improvement of SuperDARN velocity measurements by estimating the index of refraction in the scattering region using interferometry. *Journal of Geophysical Research*, *114*, A07305. https://doi.org/10.1029/2008JA013967

Gillies, R. G., Hussey, G. C., Sofko, G. J., Ponomarenko, P. V., & McWilliams, K. A. (2011). Improvement of HF coherent radar line-of-sight velocities by estimating the refractive index in the scattering volume using radar frequency shifting. *Journal of Geophysical Research*, *116*, A01302. https://doi.org/10.1029/2010JA016043

Giordano, A. A., & Haber, F. (1972). Modeling of atmospheric noise. *Radio Science*, *7*(11), 1011–1023. https://doi.org/10.1029/RS007i011p01011

Goodman, J. M. (2005). Operational communication systems and relationships to the ionosphere and space weather. *Advances in Space Research*, *36*(12), 2241–2252.

Greenwald, R. A., Baker, K. B., Dudeney, J. R., Pinnock, M., Jones, T. B., Thomas, E. C., et al. (1995). DARN/SuperDARN: A global view of the dynamics of high-latitude convection. *Space Science Reviews*, *71*, 761–796. https://doi.org/10.1007/BF00751350

Greenwald, R. A., Baker, K. B., Hutchins, R. A., & Hanuise, C. (1985). An HF phased-array radar for studying small-scale structure in the high-latitude ionosphere. *Radio Science*, *20*, 63–79. https://doi.org/10.1029/RS020i001p00063

Hargreaves, J., Ranta, H., Ranta, A., Turunen, E., & Turunen, T. (1987). Observations of the polar cap absorption event of February 1984 by the EISCAT incoherent scatter radar. *Planetary and space science*, *35*(7), 947–958. https://doi.org/10.1016/0032-0633(87)90072-9

Hargreaves, J. K., Shirochkov, A. V., & Farmer, A. D. (1993). The polar cap absorption event of 19–21 March 1990: Recombination coefficients, the twilight transition and the midday recovery. *Journal of Atmospheric and Terrestrial Physics*, *55*(6), 857–862. https://doi.org/10.1016/0021-9169(93)90026-U

Headrick, J. M., & Anderson, S. J. (2008). *Radar Handbook*, chap. HF over-the-horizon radar (vol. 34, pp. 24.1–24.43). New York: McGraw-Hill.

Hughes, J. M., Bristow, W. A., Greenwald, R. A., & Barnes, R. J. (2002). Determining characteristics of HF communications links using SuperDARN. *Annales de Geophysicae*, *20*, 1023–1030. https://doi.org/10.5194/angeo-20-1023-2002

Jones, J. B. L., Bentley, R. D., Hunter, R., Iles, R. H. A., Taylor, G. C., & Thomas, D. J. (2005). Space weather and commercial airlines. *Advances in Space Research*, *36*(12), 2258–2267. https://doi.org/10.1016/j.asr.2004.04.017

Kallenrode, M.-B. (2003). Current views on impulsive and gradual solar energetic particle events. *Journal of Physics G: Nuclear and Particle Physics*, *29*(5), 965. https://doi.org/10.1088/0954-3899/29/5/316

Kavanagh, A. J., Marple, S. R., Honary, F., McCrea, I. W., & Senior, A. (2004). On solar protons and polar cap absorption: constraints on an empirical relationship. *Annales de Geophysicae*, *22*(4), 1133–1147. https://doi.org/10.5194/angeo-22-1133-2004

Knipp, D. J., Ramsay, A. C., Beard, E. D., Boright, A. L., Cade, W. B., Hewins, I. M., et al. (2016). The May 1967 great storm and radio disruption event: Extreme space weather and extraordinary responses. *Space Weather*, *14*, 614–633. https://doi.org/10.1002/2016SW001423

Kossey, P. A., Turtle, J. P., Pagliarulo, R. P., Klemetti, W. I., & Rasmussen, J. E. (1983). VLF reflection properties of the normal and disturbed polar ionosphere in northern Greenland. *Radio science*, *18*(6), 907–916. https://doi.org/10.1029/RS018i006p00907

Kress, B. T., Mertens, C. J., & Wiltberger, M. (2010). Solar energetic particle cutoff variations during the 29–31 October 2003 geomagnetic storm. *Space Weather*, *8*, S05001. https://doi.org/10.1029/2009SW000488

Lester, M. (2013). The Super Dual Auroral Radar Network (SuperDARN): An overview of its development and science. *Advances in Polar Science*, *24*, 1–11.

Little, C. G., & Leinbach, H. (1959). The riometer—A device for the continuous measurement of ionospheric absorption. *Proceedings of the IRE*, *47*(2), 315–320. https://doi.org/10.1109/JRPROC.1959.287299

Mendillo, M., & Evans, J. V. (1974). Incoherent scatter observations of the ionospheric response to a large solar flare. *Radio Science*, *9*(2), 197–203. https://doi.org/10.1029/RS009i002p00197

Milan, S., Davies, J., & Lester, M. (1999). Coherent HF radar backscatter characteristics associated with auroral forms identified by incoherent radar techniques: A comparison of CUTLASS and EISCAT observations. *Journal of Geophysical Research*, *104*(A10), 22,591–22,604. https://doi.org/10.1029/1999JA900277

Milan, S. E., Hosokawa, K., Lester, M., Sato, N., Yamagishi, H., & Honary, F. (2008). D region HF radar echoes associated with energetic particle precipitation and pulsating aurora. *Annales de Geophysicae*, *26*(7), 1897–1904. https://doi.org/10.5194/angeo-26-1897-2008

Milan, S. E., Jones, T. B., Robinson, T. R., Thomas, E. C., & Yeoman, T. K. (1997). Interferometric evidence for the observation of ground backscatter originating behind the CUTLASS coherent HF radars. *Annales de Geophysicae*, *15*(1), 29–39. https://doi.org/10.1007/s00585-997-0029-y

NASA, GOES N Data book (2006). CDRL PM-1-1-03, Revision B, February 2005. Retrieved from https://goes.gsfc.nasa.gov/text/goes.databookn.html

Patterson, J. D., Armstrong, T. P., Laird, C. M., Detrick, D. L., & Weatherwax, A. T. (2001). Correlation of solar energetic protons and polar cap absorption. *Journal of Geophysical Research*, *106*(A1), 149–163. https://doi.org/10.1029/2000JA002006

Ponomarenko, P. V., Iserhienrhien, B., & St.-Maurice, J.-P. (2016). Morphology and possible origins of near-range oblique HF backscatter at high and midlatitudes. *Radio Science*, *51*(6), 718–730. https://doi.org/10.1002/2016RS006088

Ponomarenko, P. V., Koustov, A. V., St-Maurice, J. P., & Wiid, J. (2011). Monitoring the *F*-region peak electron density using HF backscatter interferometry. *Geophysical Research Letters,38*, L21102. https://doi.org/10.1029/2011GL049675

Ponomarenko, P. V., Menk, F. W., & Waters, C. L. (2003). Visualization of ULF waves in SuperDARN data. *Geophysical Research Letters*, *30*(18), 1926. https://doi.org/10.1029/2003GL017757

Ranta, H., Yamagishi, H., & Stauning, P. (1995). Twilight anomaly, midday recovery and cutoff latitudes during the intense polar cap absorption event of March 1991. *Annales de Geophysicae*, *13*(3), 262–276. https://doi.org/10.1007/s00585-995-0262-1

Reames, D. V. (1999). Particle acceleration at the Sun and in the heliosphere. *Space Science Reviews*, *90*(3-4), 413–491. https://doi.org/10.1023/A:1005105831781

Reid, G. C., & Leinbach, H. (1959). Low-energy cosmic-ray events associated with solar flares. *Journal of Geophysical Research*, *64*(11), 1801–1805. https://doi.org/10.1029/JZ064i011p01801

Reid, G., & Leinbach, H. (1961). Morphology and interpretation of the great polar cap absorption events of May and July, 1959. *Journal of Atmospheric and Terrestrial Physics*, *23*, 216–228. https://doi.org/10.1016/0021-9169(61)90047-2

Ribeiro, A. J., Ruohoniemi, J. M., Ponomarenko, P. V., Clausen, L. B. N., Baker, J. B. H., Greenwald, R. A., et al. (2013). A comparison of SuperDARN ACF fitting methods. *Radio Science*, *48*(3), 274–282. https://doi.org/10.1002/rds.20031

Rosenberg, T. J., Detrick, D. L., Venkatesan, D., & van Bavel, G. (1991). A comparative study of imaging and broad-beam riometer measurements: The effect of spatial structure on the frequency dependence of auroral absorption. *Journal of Geophysical Research*, *96*(A10), 17,793–17,803. https://doi.org/10.1029/91JA01827

Rostoker, G., Samson, J. C., Creutzberg, F., Hughes, T. J., McDiarmid, D. R., McNamara, A. G., et al. (1995). CANOPUS—A ground-based instrument array for remote sensing the high latitude ionosphere during the ISTP/GGS program. *Space Science Reviews*, *71*(1), 743–760. https://doi.org/10.1007/BF00751349

Ruohoniemi, J. M., & Baker, K. B. (1998). Large-scale imaging of high-latitude convection with Super Dual Auroral Radar Network HF radar observations. *Journal of Geophysical Research*, *103*(A9), 20,797–20,811. https://doi.org/10.1029/98JA01288

Sarno-Smith, L. K., Kosch, M. J., Yeoman, T., Rietveld, M., Nel, A., & Liemohn, M. W. (2016). Ionospheric electron number densities from CUTLASS dual-frequency velocity measurements using artificial backscatter over EISCAT. *Journal of Geophysical Research: Space Physics*, *121*, 8066–8076. https://doi.org/10.1002/2016JA022788

Sauer, H. H., & Wilkinson, D. C. (2008). Global mapping of ionospheric HF/VHF radio wave absorption due to solar energetic protons. *Space Weather*, *6*, S12002. https://doi.org/10.1029/2008SW000399

Schumer, E. A. (2009). Improved modeling of midlatitude *D*-region ionospheric absorption of high frequency radio signals during solar X-ray flares (Ph.D. thesis), Air Force Institute of Technology Wright-Patterson Air Force Base, Ohio, USA. http://www.dtic.mil/dtic/tr/fulltext/u2/a516063.pdf

Sterne, K. T., Greenwald, R. A., Baker, J. B. H., & Ruohoniemi, J. M. (2011). Modeling of a twin terminated folded dipole antenna for the Super Dual Auroral Radar Network (SuperDARN). In *Radar Conference (RADAR), 2011 IEEE,* pp. 934–938. https://doi.org/10.1109/RADAR.2011.5960673

Watanabe, D., & Nishitani, N. (2013). Study of ionospheric disturbances during solar flare events using the SuperDARN Hokkaido radar. *Advances in Polar Science*, *24*(1), 12–18.

Wenzel, D., Jakowski, N., Berdermann, J., Mayer, C., Valladares, C., & Heber, B. (2016). Global ionospheric flare detection system (GIFDS). *Journal of Atmospheric and Solar-Terrestrial Physics*, *138*, 233–242. https://doi.org/10.1016/j.jastp.2015.12.011